Journal of Materials Chemistry A

ROYAL SOCIETY OF CHEMISTRY

PAPER

View Article Online
View Journal

Cite this: DOI: 10.1039/d5ta05024c

Lignin for sustainable electronics: the interplay of structure, morphology and chemistry in modelling dielectric properties

Marianna Ambrico, [a] Ofelia Durante, [*b] Sebastiano De Stefano, [b] Rosarita D'Orsi, [c] Domenico Aceto, [a] Paolo Francesco Ambrico, [a] Nadia Martucciello, [d] Filippo Giubileo, [d] Sandra Rivas, [e] Alessandra Operamolla [*c] and Antonio Di Bartolomeo [b]

The search for promising and sustainable materials for advanced electronic applications has recently drawn attention to lignin. As a major by-product of pulping processes, lignin features a complex aromatic structure, rich in aliphatic and aromatic ethers, as well as hydroxyl and carboxyl functional groups, which endow it with unique chemical and electronic properties. In this study, we present a comparative analysis of three distinct lignins. Two of them (**L1** and **L2**) are derived from the Kraft pulping process, while the third (**L3**) is extracted from *Cynara cardunculus* using an ethanolic organosolv method. These lignins are investigated as active layers in an interdigitated electronic device. To explore in depth the influence of the compositional, structural, morphological and chemical properties of the three lignins on dielectric relaxation dynamics and charge transport mechanisms, several advanced analytical techniques were adopted, including Electrochemical Impedance Spectroscopy (EIS), Nyquist Plots (NP), Broadband Dielectric Spectroscopy (BDS), and Complex Power (CP) representations. Our consistent workflow included the same interdigitated electrode (IDE) platform, identical frequency window, a unified BDS formalism, and a common base EIS circuit design tailored to the observed Nyquist Plot features. Our findings revealed that the extraction process enables tuning of the lignin properties. Whilst **L1** exhibited smooth, compact morphology and a higher polymerization degree, limiting charge mobility and resulting in inferior electrical and capacitive performance, **L2** featured a fibrous structure with higher content in carboxyl groups and ashes, which significantly enhanced the conductivity and capacitance. **L3** displayed an intermediate morphology with a high concentration of aliphatic hydroxyl groups, offering a balanced blend of chemical and structural properties. In this work, we reveal the potential of lignin as a versatile dielectric material exhibiting supercapacitive behavior among other properties.

Received 20th June 2025
Accepted 21st October 2025

DOI: 10.1039/d5ta05024c

rsc.li/materials-a

1 Introduction

Lignin accounts for approximately 20–30% of the dry weight of lignocellulosic biomass[1] and constitutes a renewable resource for a variety of cutting-edge applications. The unique physicochemical properties of lignin, such as its thermal stability and redox activity, make it an attractive candidate in different fields.[2,3] However, the structural complexity of lignin offers both opportunities and challenges for its utilization. Lignin's high content of aromatic and phenol groups imparts strong antioxidant and redox properties, which are essential for energy storage devices such as supercapacitors and batteries.[4–6] Studies have demonstrated that incorporating lignin into electrodes not only improves their electrochemical performance but also reduces production costs and environmental impact, aligning with the principles of green chemistry.[7–9] Moreover, lignin-derived activated carbons, carbon nanofibers, and mesoporous carbons have emerged as leading candidates for electrode materials.[10] Furthermore, lignin has garnered attention for its intrinsic dielectric and capacitive properties.[11,12] As an amorphous polymer with a complex network of aromatic rings and ether linkages, lignin exhibits dielectric behavior suitable for use in memory devices. For example, lignin-based resistive switching random access memory (RRAM) devices have shown promise for high-density information storage, leveraging lignin's ability to form multilevel resistance states.[13,14] Recent

[a]CNR – ISTP, Institute for Plasma Science and Technology, Via Giovanni Amendola 122/d, Bari 70126, Italy

[b]Department of Physics "E.R. Caianiello", University of Salerno, Via Giovanni Paolo II 132, Fisciano, (Sa) 84084, Italy. E-mail: odurante@unisa.it

[c]Department of Chemistry and Industrial Chemistry, University of Pisa, Via Giuseppe Moruzzi 13, Pisa 56124, Italy. E-mail: alessandra.operamolla@unipi.it

[d]CNR-SPIN, Salerno Unit, Via Giovanni Paolo II 132, Fisciano, (Sa) 84084, Italy

[e]Department of Chemical Engineering, Faculty of Science of Ourense, University of Vigo, As Lagoas s/n, 32004 Ourense, Spain

studies have also demonstrated the potential of lignin as a gate dielectric material in organic field-effect transistors (OFETs).[7,15] Specifically, Kraft lignin has shown promising results as a dielectric layer in bottom-gate OFETs, offering reliable electrical performance along with environmentally friendly characteristics.[7] On the other hand, lignin extracted through the organosolv process – known for its higher purity and better solubility in organic solvents – has yet to be explored for use in electronic devices. From a broader perspective, Kraft pulping and organosolv extraction represent contrasting technological and sustainability paradigms. Kraft pulping is primarily designed to delignify biomass or cellulose fiber recovery, producing lignin as a byproduct along with sulfur-containing residues, degraded carbohydrates and inorganic salts. These lignins are heterogeneous, partially condensed and contain residual inorganic compounds.[16] In contrast, organosolv processes use organic solvents under milder conditions, yielding higher-purity lignin with lower sulfur content, more defined hydroxyl functionality and improved solubility for high-value applications. From a sustainable perspective, Kraft pulping is cost-effective and scalable but generates chemical effluents, whereas organosolv processes offer environmental advantages despite higher production costs. Then, the choice of extraction method fundamentally influences both the structural and chemical characteristics of lignin, which in turn dictate its technological performance across diverse applications. **L1**, **L2** and **L3** were deliberately chosen to encompass a relevant technological spectrum. **L1** and **L2** are widely available from industrial pulping processes, while the biomass-derived organosolv **L3** introduces a higher-purity variant with enhanced functional accessibility.[17]

Many factors influence the electrical behavior of lignin, which are encountered only to a limited extent in synthetic organic polymers. Lignin is a random copolymer of *p*-coumaryl, coniferyl and sinapyl alcohols,[18,19] for which there is limited knowledge about its chemical connectivity, especially in terms of the true sequence of the repeating units. This makes even theoretical predictions of lignin properties, in terms of self-aggregation, highly difficult. Furthermore, the extraction methods used for lignin isolation leave a fingerprint over the isolated material, which involves the presence of impurities in the isolated product[20,21] and molecular skeleton modification. Often, technical lignins contain ashes or residual proteins or sugars; nonetheless, many other studies apply lignin in electronic devices without correlating the performance with the eventual presence of impurities, which, in some cases, may not be negligible.[5,8,11,22]

This study aims to be a follow up of previous study on three lignins: two of them (**L1** and **L2**) sourced from the Kraft pulping process and one (**L3**) derived from *Cynara cardunculus* using an organosolv extraction method.[23] All samples are solution-processed under identical conditions to ensure consistency. Due to their distinct chemical compositions and extraction methods, the three lignins exhibit varied ash and functional group content (phenolic and aliphatic OH, carboxyl groups, sulfur content *etc.*) and aggregation behaviors, which in turn influence their device performance and are parametrized in this study to identify factors allowing the assessment of lignin pathways to valorization in electronic devices. In this context, the adoption of Electrochemical Impedance Spectroscopy (EIS) and Broadband Dielectric Spectroscopy (BDS) has proven particularly suitable for providing insights into the correlation of the complex polymeric nature, morphology and chemistry of lignins with their charge carrier storage and transport properties. These insights are crucial for evaluating their potential applications in various electronic and energy storage devices. Unlike the DC current–voltage response, EIS and BDS rely on the response under an AC field which enables the capture of signals from polymeric chains oscillations, ionic charge current and distributions, as well as redox reaction signals.[24–29] In summary, this study sheds light on the different properties of lignin that can be fine-tuned for selecting the production process. We aim to offer new insights, positioning lignin as a versatile material for future dielectric and energy storage applications.

2 Results and discussion

2.1 AC electrical characterization

Solutions of the three lignins were prepared in EtOH:NH_4OH in a 1:1 volumetric ratio at 20 mg mL^{-1} concentration. The solutions were drop-cast onto circular Ti/Au interdigitated electrodes (IDEs) (MICRUX; $\varnothing = 3.5$ mm, 90 finger pairs, and 90 μm width/gap) under ambient conditions (20 °C and 50% RH). More information on the morphological, chemical and structural properties of the materials is reported in Table S1, Fig. S1 and S2 of the SI and in ref. 30. Prior to deposition, the suspension was stirred for 5 minutes at 2000 rpm, and the electrodes were ultrasonically cleaned in isopropyl alcohol and dried in air; all depositions were performed in triplicate to ensure reproducible impedance responses. Replicate depositions produced overlapping spectra and measured film thicknesses around 0.35–0.40 μm by atomic force microscopy (RMS roughness, ~107 nm).[13]

2.1.1 Nyquist plots. Electrochemical impedance spectroscopy (EIS) uses the Nyquist plot (NP) representation of the impedance Z, where the x-axis represents the real part of the impedance (ReZ), indicative of the resistance of the system. The y-axis represents the imaginary part of the impedance ($-$ImZ) that is associated with the capacitive properties of the system. In a NP representation, the frequency decreases from the left to the right of the plot, and the behavior is represented *via* a specific combination of electrical circuital components.[31] More details on the features of the circuit elements adopted in this work and their response *vs.* the AC frequency are shown in Fig. S3 of the SI.

In Fig. 1, we report the experimental (symbols) and best-fit (straight lines) NP spectra in the full frequency range (1.0 MHz–0.1 Hz from left to right) at 0.0 V and at ±0.8 V for **L1** (Fig. 1a), **L2** (Fig. 1b), and **L3** (Fig. 1c) on IDE devices together with the equivalent circuits simulating the experimental data at both DC voltages (Fig. 1d and e). The values of the circuit parameters extracted using the EIS analyzer software[32] are summarized in Table S2 of the SI. The choice of applied DC

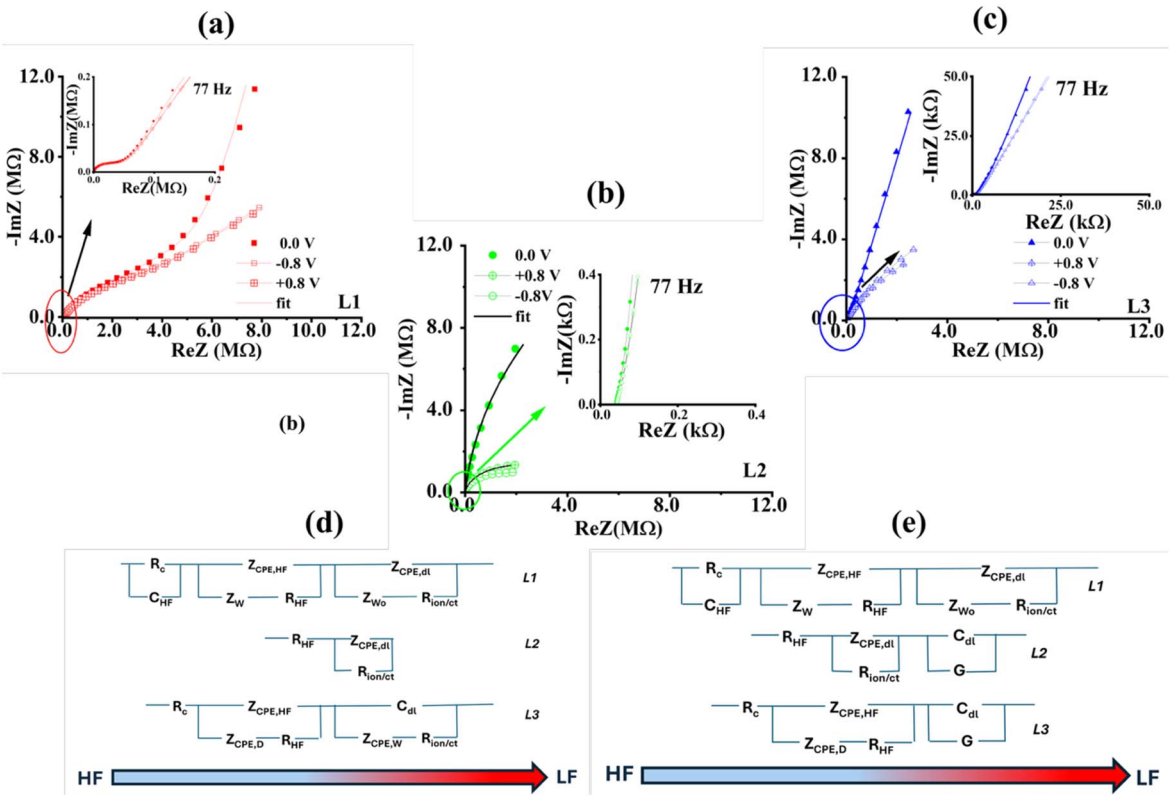

Fig. 1 Impedance spectroscopy representation *via* Nyquist plots for devices **L1** (a), **L2** (b), and **L3** (c) from 1 MHz to 0.1 Hz, at 0.0 V and with a bias of ±0.8 V DC. The insets show the high and medium frequency range (1 MHz–77 Hz). The equivalent circuits (d and e) model the electrical behaviour at 0.0 V (d) and ±0.8 V (e). The arrows indicate the active components at high (HF) and low frequencies (LF). In **L2** and **L3**, the Gerischer impedance (G) appears at ±0.8 V, suggesting chemical reactions prior to the oxidation–reduction processes.[33] The electrical circuits simulating the NPs were built up by using the EIS analyzer software.[34]

polarization (0.0 V and ±0.8 V) was made to exclude from the electrochemical window the redox potential of water, ensuring the assessment of the electrical symmetry of the device at positive and negative voltages. This allowed us to study the potential charge transfer processes and the possible occurrence of redox activity, with regard to ionic and electronic transport mechanisms.

A preliminary insight into the full NP behavior at 0.0 V_{DC} revealed significant differences in the **L1** device with respect to the **L2** and **L3** devices, which were mainly visible in the low-frequency range (Fig. 1a–c, right side of the plot). Moreover, **L2** exhibits a distinctive feature, with a low resistance at high frequency and the sharp onset of a dominant capacitive contribution toward lower frequency. The NP magnifications (insets of Fig. 1a–c for high and medium frequencies and Fig. S4 in the SI) revealed other specific fingerprints *vs.* the frequency, not visible in the full spectra, and allowed capturing differences and similarities in the AC response among the three lignin devices.

At higher frequencies, **L1** (Fig. 1a inset and S4) and **L3** (Fig. 1c inset) show comparable electrical behavior, whereas **L2**'s response (Fig. 1b) is essentially dominated by a small resistance and, again, by the onset of capacitive behavior. Furthermore, this is characterized by a sharp increase in ImZ, yielding a curve almost parallel to the y-axis, a trend generally observed in supercapacitors.[35] Notably, the module of the experimental impedance $|Z|$ and, more specifically, the values at high frequency of the real part ReZ due to the only resistive response pass from 20 kΩ in **L1** to 887 Ω in **L3** and 46 Ω in **L2** (see Fig. S4 in the SI), justifying the DC currents observed in the *I–V* characterization studies.[30]

Following the experimental evidence, **L1** and **L3** can be modeled by similar equivalent circuit structures, whereas a different model is required for **L2**. Notably, similar behavior is present at both positive V_{DC} = +0.8 V and negative V_{DC} = −0.8 V because of the almost ohmic behavior of the Au IDE contacts. Therefore, we focus our attention on cases in which V_{DC} = 0.0 V and V_{DC} = +0.8 V. In this approach, the NP behavior (either 0.0 V_{DC} or V_{DC} = ±0.8 V) can be described by two main sections: the first extends in the frequency range of 1.0 MHz–77 Hz (high–mid-frequency region) and the second extends from 77–0.1 Hz (mid–low-frequency region). Details on the development of various regions of spectra represented per frequency decade and justifying the modeling are reported in Fig. S4 of the SI.

At V_{DC} = 0.0 V, modeling the NPs was performed using the free downloadable EIS analyzer software,[36] and the equivalent electrical circuits are shown in Fig. 1d for **L1**, **L2** and **L3**, respectively. The components are arranged in the order of frequency, starting from the high-frequency (HF) region on the left and progressing to the low-frequency (LF) region on the

right. The equivalent circuits applicable at $V_{DC} = \pm 0.8$ V are summarized in Fig. 1e.

For **L1** (Fig. 1a) and **L3** (Fig. 1c), the equivalent circuit consists of two sections made up of Randle-like circuits (Fig. 1d, the sections marked by the arrow colored from blue (HF) to red (LF)),[28] one effective in the high–mid-frequency range and the other in the low-frequency range. Compared with the AC conductivity spectra (see the next section), the first section of the circuit, covering four decades, was assigned to ionic diffusion, electrode polarization and ionic hopping, whereas the second was assigned to the lignin redox features.

In the first section, the lower branch of the Randle's circuit is associated with free ionic charge diffusion and represented by a Warburg impedance (Z_W) in **L1** and a constant phase element $Z_{CPE,D}$ in **L3**. Notably, the impedance values (see Table S1, where $Z_{CPE,D} < Z_W$) and R_{HF} in **L3** are lower than those in **L1**, suggesting that ionic charge diffusion is less hindered in **L3** compared to **L1**. A further element was added to represent the contact impedance ($R_c//C_{HF}$ in **L1**) or resistance (C_{HF} in **L3**) at the lignin/Au_{IDE} interface. In the upper branch associated with the double layer, the corresponding impedance $Z_{CPE,HF}$ is much greater in **L3** than in **L1**, an effect that appears in the former as a sharp increase along the $-\mathrm{Im}Z$ axis similar to that observed in **L2**.

The second section (low frequency, LF) represents the transport at the 'Au_{IDE} (electrode) lignin (electrolyte)' interface. The lower branch, labeled as faradaic, again includes Randle's-like circuit features *i.e.* the series of $R_{ion/ct}$ with a Warburg open (Z_{Wo}) impedance in **L1** and with a constant phase element Z_{CPE1} in **L3**. In **L1**, the adoption in the equivalent circuit of a Warburg open impedance (Z_{Wo}), rather than a semi-infinite Warburg impedance Z_W,[35,37] is justified by the presence in the NP of a straight line with a slope greater than 45° (see EIS spectra in the SI). Overall, the series of $R_{ion/ct}$ with the diffusion elements enable estimating the magnitude of charge transfer *via* redox reactions[36,38] and thereby the reactivity to the environment. Finally, in the upper branch, the constant phase element Z_{CPEdl} in **L1** and a capacitor C_{dl} term in **L3** are placed parallel to the faradaic one and represent the charge double layer forming at the electrode/lignin interface.

L2 (Fig. 1b) behavior stands out from **L1** and **L3**: here, the first section representing the NP consisted of a resistor named $R_{HF,}$ corresponding to the intercept on the ReZ. The second section consists of the parallel of the double layer nonideal capacitance $Z_{CPE,dl}$ and of the ionic charge resistance $R_{ion/ct}$, as representative of the dominant extension of the impedance along the $-\mathrm{Im}Z$. Moreover, $R_{ion/ct}$ is an index of the ability of the ionic charge to promote charge transfer (*via* redox reactions) at the electrodes. Notably, this circuit is typically encountered when simulating the NP of supercapacitor devices.[35]

Finally, we found that the Z_{CPEdl} in **L3** places in between those of **L1** and **L2** (see Table S2 in the SI), and the high-frequency resistance decreases in the order of R_{HF}(**L1**) > R_{HF}(**L3**) > R_{HF}(**L2**) (see Table S2 in the SI), in agreement with the magnitude of the measured DC currents. Similarly, this sequence can be explained because of the features of the morphological structure shown in Fig. S1.

In all the three lignin devices, the superposition of a DC bias (either positive or negative) to the AC one modified their response at low frequencies, although the extent of the response varied significantly. These changes can result, for example, from redox reactions at the electrode/lignin interface, producing charge transfer currents whose magnitude is represented by the resulting values of the charge transfer resistance $R_{ion/ct}$ under bias.

Again, in this range, **L2** and **L3** demonstrated a DC vehiculated response represented by the presence in **L2** either of a lower $R_{ct/ion}$ ($R_{ct/ion} = 3.5 \times 10^7$ Ω at 0.0 V and $R_{ct/ion} = 1.2 \times 10^6$ Ω at 0.8 V, see Table S2 in the SI) or a Gerisher impedance[33] and in **L3** of a solely Gerisher impedance. Therefore, these results further confirm the higher reactivity of both lignins due to the presence of adsorbates, as also suggested by the *I–V* measurement under different pressures.[30] The latter is furthermore indicative of mixed, albeit not distinguishable, electronic–ionic conduction due to a peculiar charge exchange current at the electrode/lignin interface, which is consistent with the occurrence of diffusion coupled with chemical reactions.[33] Conversely, in the low-frequency section, when a bias is applied, the **L1** device retains the same behavior, as expressed by the similar order of magnitude of the values of $R_{ion/ct}$ in Randle's circuit and hints at lower or null reactivity, which is accompanied by a localized ionic charge diffusion mechanism expressed again by the Z_{W0} impedance element.

To summarize, at 0.0 V, **L1** and **L2** display peculiar circuits, the former being a superposition of HF and LF transport ascribed to ionic charge-free diffusion and redox properties at the lignin interface; conversely, **L2** displays a sharp and fast transition from a low impedance (resistive state) to a quasi-ideal capacitive state covering the full frequency. The circuit of lignin **L3** is similar to that of **L1** at high frequencies, whereas, at low frequencies, the electrical properties of **L3** are dominated by capacitive effects. The behavior can be interpreted in strict relation to morphology. The similarities of **L2** and **L3** increase at 0.8 V, indicating their interaction with the external environment. Indeed, the presence of a Gerisher impedance hints at more reactivity toward ambient gases.

2.2 Broadband dielectric spectroscopy (BDS) results

The BDS is recognized as a powerful data representation for accessing impedance properties of polymeric materials,[39–42] highlighting the molecular dynamics of materials in response to an AC field. In this framework, BDS allows investigating in great detail the dielectric relaxation processes and AC charge transport at various time scales.[25,43] Details on the mathematical formalism used in this section are provided in the SI.

We found that the lignin polymer structure, morphology and chemistry strongly affect the permittivity $\varepsilon(\omega)$ (eqn (S8)) and AC conductivity $\sigma(\omega)$ (eqn (S12)) frequency dispersion features. The $D_{\ln\omega}\varepsilon'(\omega)$ Kramers–Kronig representation of the permittivity $\varepsilon'(\omega)$ (eqn (S10)) is more suitable to enhance the elicited features *via* the presence of more resolved peaks at frequencies typical for specific lignin relaxation mechanisms.[41,44] As a result, in **L1** (panel 2a, red curve), the first peak is due to β-relaxation and

can be associated with the hydration status of the polymer[45] or the radial charge hopping mechanism,[13,24] and the second peak is due to electrode polarization (EP). An additional relaxation process is observed and attributed to near-constant loss (NCL).[42] Unlike **L1**, the $D_{\ln\omega}\varepsilon'(\omega)$ of **L2** (panel 2a, green curve) exhibits a dominant relaxation process, hinting an extended EP and a rise toward lower frequencies. However, in our previous findings, the measurements conducted on **L2** down to 1.0 mHz[13] revealed the presence of two more peaks. The first one is termed α-relaxation and commonly associated with the polymeric chain length, *i.e.* the longer the chain, the lower the oscillation frequency;[45] moreover, it can be qualitatively associated with the polymerization degree and/or polymer aggregate dimension.[24,25] The second peak is again representative of the elicited β-relaxation. Like **L1**, **L3** (panel 2a, blue curve) displays two distinct peaks in $D_{\ln\omega}\varepsilon'(\omega)$, corresponding to β-relaxation and EP, the latter extending less in frequency than in **L2**.[46] Additionally, in **L3**, α relaxation occurs at frequencies slightly higher than **L2**, which implies a lower extension of the polymer aggregates.[47] The observed frequency location of the α-relaxation confirms what is already discussed in our previous paper, *i.e.* due to the extraction process, the degree of polymerization scales down going from **L1** to **L2** and **L3**.

The inspection of the AC conductivity enables recognition of two distinct regions in **L1**'s σ' plot (red trace in panel 2b), both following Jonsher–Funke's law[48] (see eqn (S12) in the BDS data analysis section), where the power term, *i.e.*, $A\omega^n$ with $n<1$, has $n \sim 0.7$ at frequencies <1.0 kHz and $n \sim 0.5$ at higher frequencies. These correspond in $D_{\ln\omega}\varepsilon'(\omega)$ to the β-relaxation and the EP, respectively. The crossover region is linearly dependent on the frequency ($B\omega$, eqn (S10)), validating the NCL relaxation observed in $D_{\ln\omega}\varepsilon'(\omega)$.[49] In **L2** (panel 2b, green curve), the behavior is noticeably distinct from the one of **L1**. **L2**'s previously reported n values[13] prove that charge hopping occurs mainly through localized trap states ($A\omega^n$, $n \cong 1$, *i.e.*, $n = 0.85$ up to 200 Hz and $n = 1.43$ up to 10 kHz)[50] and is followed by free ion charge diffusion, evidenced by a short curve plateau. **L3**'s conductivity behavior (panel 2b, blue curve) is intermediate between that of **L2** and **L1**: at low frequencies, it follows Funke's law (with $n \approx 1$, specifically $n = 0.92$) as **L2**'s, whereas at high frequencies it conforms to Johnsher's law ($n = 0.41$) and the Nearly Constant Loss (NCL) region as **L1**'s.

It is interesting to note the correlation of these findings with the three lignin morphologies. Fig. S1 shows the field emission scanning electron microscopy (FE-SEM) micrographs of the three lignins. **L1** produced smooth, amorphous films with flat surfaces, reflecting its high solubility and lack of aggregate formation due to a high free phenol group content. In contrast, **L2** showed a rough surface with fibrous structures and agglomerates, which is attributed to its lower solubility. **L3** exhibited an intermediate morphology with some agglomerates and a rougher surface than **L1**, but better dispersion than **L2** due to its higher content of aliphatic hydroxyl groups, which facilitate hydrogen bonding with the solvent. It is noteworthy how the n values correlate strictly with the morphological structure, with $n<1$ in **L1**, which displays a smoother homogeneous surface as observed in amorphous materials, favoring delocalized ionic charge hopping transport mechanisms, and $n \geq 1$ in **L2**, which displays a more inhomogeneous structure, favoring more localized charge transport.[50] In **L3**, the presence of grains and grain boundaries explains the n value in the middle between those in **L1** and **L2**. Furthermore, the values of σ' at the plateau ($\sigma_{DC,HF}$)follow the sequence $\sigma_{DC,HF}$ (**L1**) (10^{-7} S cm^{-1}) < $\sigma_{DC,HF}$ (**L3**) (10^{-5} S cm^{-1}) (**L1**) < $\sigma_{DC,HF}$ (**L2**) (10^{-4} S cm^{-1}), in line with the R_{HF} one derived from NP simulation and from the DC RT current–voltage measurements.[30]

The loss factors tan δ (panel 2c) connect the permittivity and conductivity results. In **L1**, tan δ (red curve in Fig. 2c) features two well-resolved peaks, corresponding to the β-relaxation and EP, and confirming that the AC conductivity occurs through a superposition of two different ionic charge hopping mechanisms *via* delocalized states.[48,51] Interestingly, in **L2**, the loss factor representation (green curve in Fig. 2c) presents the tail of a peak at a frequency much lower than 0.1 Hz, which we referred to as the α-relaxation, accompanied by a small bump signaling the β-relaxation and a tail refering to the EP relaxation. In **L3**, the loss factor (blue curve in Fig. 2c) exhibits a behavior more similar to **L1** than to **L2**, exhibiting only two visible peaks, corresponding to the β-relaxation and EP, with no evidence of the α-relaxation (Fig. 2a). This aspect, with respect to the Kramers–Kronig representation, is justified by the DC conductivity contribution to loss factor, affecting the resolution of all the relaxation peaks, especially those at low frequencies.[41] The conductivity $\sigma_{DC,HF}$ (Fig. 2e, left y-axis) and mobility μ_{HF} (2e, right y-axis) values at the plateau correlate with the COOH (Fig. S6b and d) and phenolic group OH(Φ) (Fig. S6a and c) millimolar content of lignin. The values of $\sigma_{DC,HF}$ and μ_{HF} increase by approximately two orders of magnitude in the order **L1** < **L3** < **L2**. These parameters are plotted *vs.* the COOH/phenolic OH molar ratio (COOH/OH(Φ), Fig. 2d) which increase in the same order. The two chemical functionalities exert a competitive effect on conductivity parameters: the COOH group provides H^+ protons as diffusive ionic charges, whilst the phenolic OH increases the pseudocapacitive behavior. Conversely, at low frequencies, where localized hopping is the main transport mechanism, the D_{LF}, and the corresponding charge mobility, μ_{LF} (Fig. 2e, eqn (S13) and (S15)) decrease in the order of **L1** < **L2** < **L3** and are found to be proportional to the polydispersity index (PDI) of the polymeric chains which decreases in the same order.

As a result, we observe the frequency shift of the α-relaxation peak in the order of **L1** < **L2** < **L3**. This correlates well with the lignin weight-average molecular weight, M_w (Table S1), in a sense that the lower the M_w the higher the frequency of the α-relaxation peak (Fig. 2f). M_w is a measure of the average mass of molecules in a sample, giving more influence on larger molecules and reflects their contribution to the α-relaxation mechanism. Finally, the mass weight M_w relates with the balance between the phenyl *vs.* aliphatic–OH, as seen in Fig. 2f. This is implicit as the higher the extent of depolymerization, the higher the number of phenolic groups liberated, and depending on the extraction method, not all of them will be balanced by aliphatic alcohols that can be subject to elimination processes.

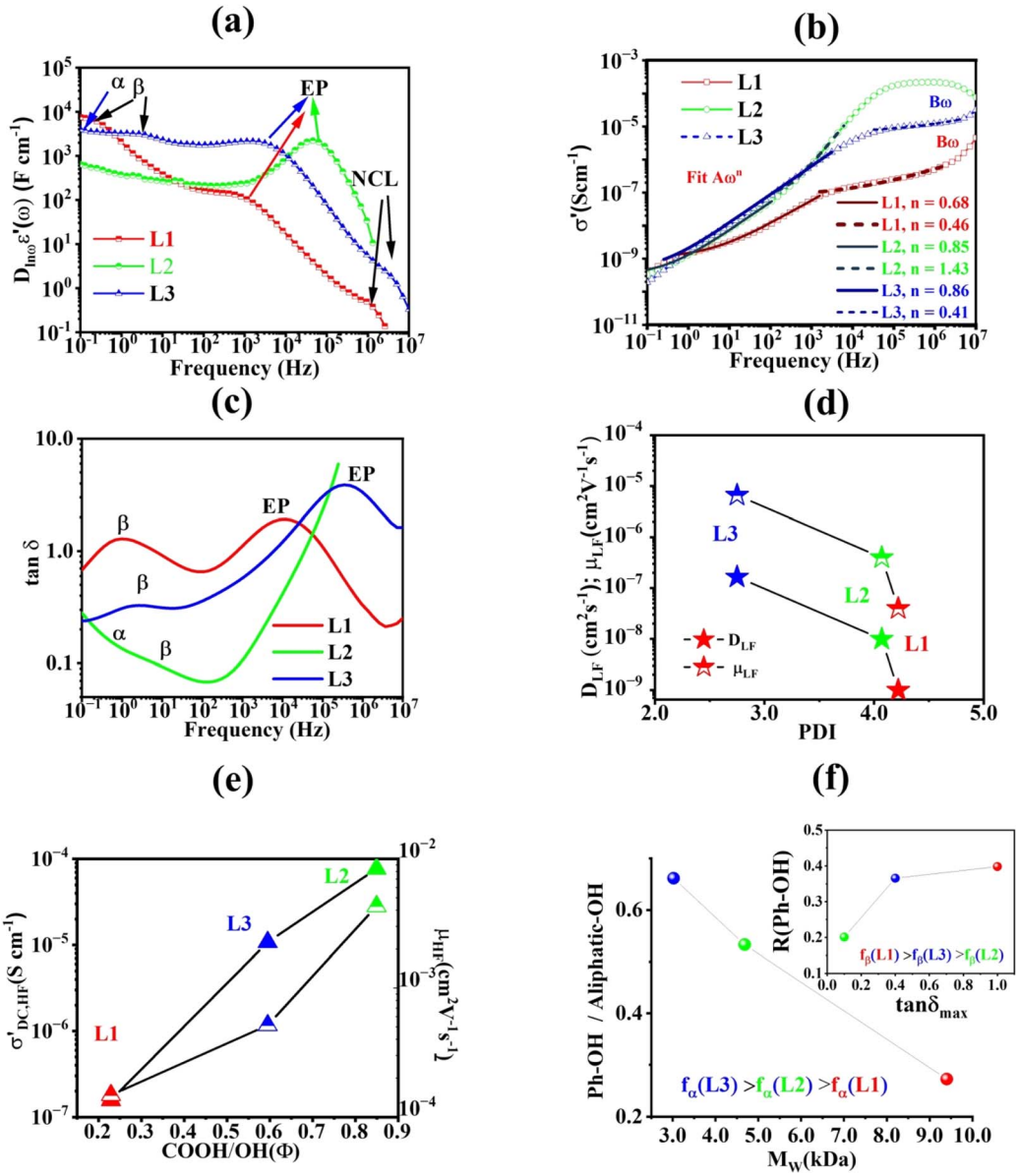

Fig. 2 (a–c) Broadband dielectric spectroscopy results of lignins **L1**, **L2**, and **L3**. (a) Dielectric response $D_{\ln\omega}\varepsilon'(\omega)$, showing α, β, EP and NCL relaxations. (b) Real part of the AC conductivity (σ') fitted with Jonscher–Funke's law $A\omega^n$ with n <1 in **L1** and n ≥1 in **L2** and **L3**. (c) Loss factor tan δ in the log–log scale, highlighting relaxation peaks. (d–f) Correlations between the BDS and chemical characterization parameters: (d) conductivity σ_{HF} (left y-axis) and mobility μ_{HF} (right y-axis) *vs.* the COOH/OH ratio from the COOH and OH contents in Table S1. (e) Low-frequency diffusion coefficient, D_{LF}, and charge mobility, μ_{LF} *vs.* PDI values in Table S1. (f) Correlation between the sequency in weight average (see Table S1) M_w (Table S1) in lignin and the ratio of the phenyl –OH (Ph–OH) *vs.* aliphatic–OH content, linked to the α-relaxation frequency shift; inset: correlation between the sequency of the ratio R = Ph–OH/(Ph–OH + aliphatic–OH) and the magnitude of the peak in loss factor tan δ related to β-relaxation in the label, with the corresponding blue shift in the β-relaxation peak position of the frequency f_β (Table S1 and Fig. 3c).

The β-type relaxation is generally attributed to the hydration level, as previously reported by Ambrico *et al.*[43] In our study, all impedance measurements were performed under controlled laboratory conditions with a consistent relative humidity of approximately 50%. Therefore, the observed β-relaxation can be interpreted in the light of hydrophilic or hydrophobic nature of the lignin samples. By analyzing the behavior of the loss factor, we observe that both the intensity and frequency position of the β-relaxation peak follow the sequence: **L1** > **L3** > **L2**. These findings suggest that a higher β-peak magnitude corresponds to a more hydrophilic character. Within this context, a strong correlation has been identified between β-relaxation and the relative content of aliphatic –OH groups. Additionally, this observation is consistent with the presence of aromatic condensation in the polymeric chains of **L2**, which contributes to its more hydrophobic nature and affects its ionic conductivity (see ref. 52 and references therein).

The chemical formula, specifically the sulfur/nitrogen (S/N) stoichiometric coefficient ratio *vs.* the ash percentages (Table S1 and Fig. S7 of the SI) suggests that **L1** and **L2** contain sulfates

in their ashes, as revealed by previous scanning electron microscopy-energy dispersive spectroscopy (SEM-EDS) analysis.[7,53] The sulfated ashes have long been known to cause a linear increase in the electrical conductivity depending on their concentration.[53] Accordingly, the higher value of the plateau in the AC conductivity in **L2** can be explained as a combined effect of the ash content (25.3%), morphology and COOH/OH (Φ) ratio. In this framework, the ash may create conducting paths in **L2** aggregates, allowing to reduce the energetic barrier to charge diffusion by the **L2** inhomogeneous morphology, also favoring a mixed ionic/electronic path. Conversely, in **L1**, the more uniform aggregate distribution favors the inter-aggregate delocalized hopping, whereas the much lower ash content and lower COOH/OH(Φ) ratio do not suggest an increase of the current due to free diffusion of ionic charges. Again, in **L3**, the conductivity falls between **L1** and **L3**. Considering the linear correlation of the ash content to the conductivity[53] and to the S/N ratio calculated from FWs (Table S1), we confirm this trend in plot S7, which is compatible with a rough estimation of ash at **L3** of ~1.5%. Therefore, we can assume that the conductivity and capacitive properties of **L3** are essentially related to those of COOH/OH(Φ) ratio.

In summary, the BDS analysis revealed that the dielectric relaxations of **L1**, **L2** and **L3** in the explored frequency range are closely related to the PDI (determining the mobility and diffusivity), to the hydration feature *via* the β-relaxation, and to the EP *via* the ion charge displacement. The lignin morphology is responsible for establishing ionic charge hopping (Jonscher–Funke's law)[50,51] with the COOH and OH (Φ) hydroxyl contents and their ratio regulating the carrier transport mechanisms, mainly free ion charge diffusion and displacement. The former, being under conditions approaching the DC *I–V* conditions, displayed conductivity values in line with those observed in the IV characteristics under a DC electric field. Moreover, a peculiar role is believed to be played by the ash content in determining mixed electronic/ionic conduction in **L2**. Within our sample set, ash content modulates both the AC conductivity plateau and the capacitive window. **L2** (25.3% ash) shows a doping-like enhancement of mixed ionic/electronic pathways, a low HF resistive intercept, and a Gerischer element under ±0.8 V, consistent with sulfate-rich ashes. Conversely, **L1** (~3.1% ash) and **L3** (ash negligible, ~1.5% estimated from S/N) fall in a low-ash regime where dielectric/capacitive properties are governed primarily by COOH/OH chemistry and morphology. Operationally, our data indicate minimal impurity impact for $\lesssim$3% ash and a marked effect in a high-ash regime ($\gtrsim$ 20%).

2.3 Supercapacitive properties of lignins: applications

The supercapacitor (SC) performance of lignin-based devices (**L1**, **L2**, and **L3**) is evaluated through the power representation of their impedances, specifically by analyzing the complex power[35]

$$S(\omega) = P_{\mathrm{Act}}(\omega) - jQ_{\mathrm{React}}(\omega).$$

of the reactive power, $Q_{\mathrm{React}}(\omega)$ and active power, $P_{\mathrm{act}}(\omega)$, calculated *via* the real $C_{\mathrm{p}}^{'}$ and imaginary $C_{\mathrm{p}}^{''}$ parts of the capacitance (Fig. 3a) and represented in Fig. 3b–d as the values normalized to the module of the power S, $|S|$ (compare SI, eqn (S16)–(S20)).

In lignin **L1** (Fig. 3b), $P_{\mathrm{act}}(\omega)$and $Q_{\mathrm{React}}(\omega)$ do not present a clear transition point from capacitive to resistive states, and multiple relaxation phenomena are driven mainly by two superimposed hopping mechanisms, limiting the development of net charge displacement and then the onset of more capacitive behavior. These behaviors reflect the structural complexity, disordered nature of **L1** and moderate ash content (3.1%), and low ionic charge mobility and summarizes confinement, which hinder supercapacitor performance (Fig. 3b). Finally, the estimated values of volumetric capacity/energy/power of the three lignins are shown in Table 1.

Moreover, considering the results in Fig. 3d and S6, the relatively high content of phenolic hydroxyls (OH(Φ) = 1.31 mmol g^{-1} of lignin) suggests a strong pseudocapacitive contribution that, together with the limited density of carboxyl groups (COOH = 0.30 mmol g^{-1} of lignin), inhibits ionic diffusion, contributing to the oscillatory behavior observed in P_{act} and Q_{React} and its reduced SC performance. On the other hand, **L2** in panel (c) exhibits a sharp capacitive-to-resistive transition at a frequency of 67 kHz, estimated at the crossover when $P_{\mathrm{act}} = Q_{\mathrm{React}}$ and corresponds to the rise time (t = 15 μs). (Fig. 3c).

At low frequencies, Q_{React} dominates, indicating efficient charge storage. The rapid transition at higher frequencies to $P_{\mathrm{act}}(\omega) > Q_{\mathrm{React}}(\omega)$, *i.e.*, from a capacitive to a low resistive behavior mimicking the DC current response, reflects excellent mixed ionic and electronic conductivity, which is further attributed to the higher ash content. Furthermore, the wide frequency range showing capacitive behavior together with the rapid transition indicate interesting SC properties. The SC performance of **L2** can be further explained as a combined effect due to its high ash content (25.3%). Furthermore, while fibrous morphologies are often advantageous for charge transport, SEM analysis of **L2** suggests a less uniform distribution of fibrous domains. This heterogeneity may introduce energy barriers to ion hopping at low frequencies, where ions must move across distant aggregates or grain boundaries. However, the high ash content (25.3%) increases the electronic conductivity, particularly at high frequencies, probably through a doping-like effect. Consequently, the synergy between fibrous morphology, hydroxyl functionality and ash content favors efficient charge transport over a wide frequency range. The balance between the phenolic hydroxyl content (OH(Φ) = 0.73 mmol g^{-1} of lignin) and the high carboxylic group density (COOH = 0.62 mmol g^{-1} of lignin) equilibrates the capacitance and ionic conductivity and supports its rapid capacitive–resistive transition and the overall SC performance. The frequency of the resistive *vs.* capacitance transition at **L3** occurs at approximately 1.0 kHz, (panel d) estimated at at f = 3.7 kHz corresponding to the crossover frequency when $Q_{\mathrm{React}} = P_{\mathrm{react}}$ at f = 3.7 kHz and t = 312 μs (Fig. 3d), which is one order of magnitude slower than that at **L2**. Like **L2**, **L3** demonstrated strong capacitive behavior at low frequencies, with dominating Q_{React}. The highest aliphatic hydroxyl content (OH = 2.90 mmol g^{-1} lignin) enhances hydration, supporting **L3**'s capacitive behavior

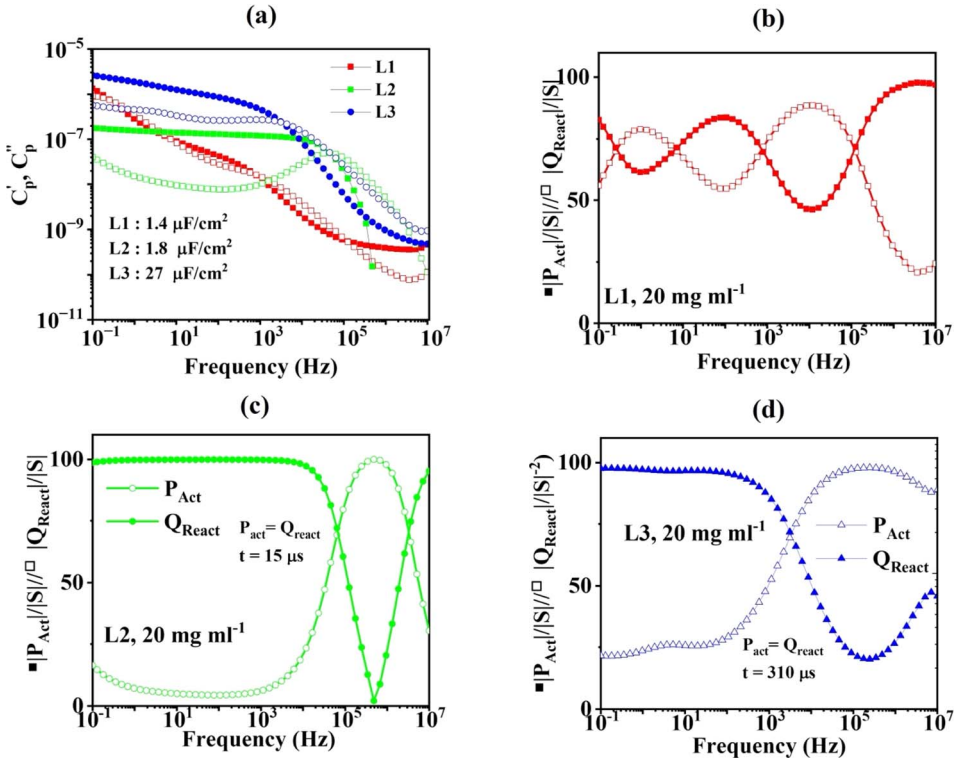

Fig. 3 (a) Values of the real C_p' (solid squares) and imaginary C_p'' (hollow squares) part *vs.* *f* of the capacitance as calculated from impedance data (expr. S16–S17). In the label, the values of the C_{areal} (Table 1) at 0.1 mHz are reported. (b) Reactive power ($Q_{React,}$ solid symbols) and active power (P_{act}, hollow symbols) normalized to the module of the complex power $S = Q_{React} + jP_{act}$ as a function of frequency for (b) **L1**, (c) **L2**, and (d) **L3**; in **L2** and **L3**, the crossover frequencies between (Q_{React}) and (P_{act}) (*i.e.* $Q_{React} = P_{act}$) were 67 kHz and 3.2 kHz, respectively, corresponding to $t = 15$ μs and $t = 310$ μs. The volumetric capacitance, energy and power densities are summarized in Table 1.[54]

at low frequencies. Moreover, the moderate phenolic hydroxyl content (OH(Φ) = 0.79 mmol g^{-1}) and intermediate carboxylic group density (COOH = 0.47 mmol g^{-1}) provide a balance between the pseudocapacitive and ionic contributions. These chemical features, combined with potential structural inhomogeneities and internal defects and an undetectable ash content, likely contribute to the slower capacitive-to-resistive transition than that of **L2**. Despite the slower transition dynamics, **L3** retains a significant SC potential because of its capacitive behavior at low frequencies and the combined effects of its hydroxyl functionalities and molecular structures. In summary, the SC performances of the three lignins **L1**, **L2** and **L3** are a consequence of the combination of chemical and morphological features, both of which contribute to tuning the onset or absence of a transition from capacitive to resistive behavior.

Operationally, **L2** sustains capacitive fast operation with the lowest HF resistance intercept, while **L3** combines robust LF capacitance with cleaner chemistry, two distinct, application-relevant profiles. Notably, the areal and volumetric capacitance values – consistent with recent benchmarks – combined with an extended frequency range and energy conversion efficiency surpassing 95% establish a strong and promising foundation for future sustainable, high-speed lignin-based microsupercapacitor device engineering. However, targeted efforts to enhance energy and power densities remain essential to fully unlock their potential.

Table 1 Areal and volumetric capacitance, energy and power densities estimated at 0.1 Hz for the three lignins and Q_{React}/P_{act} crossover frequencies

Item	C_{areal} [b] (μF cm^{-2})[a]	C_{Vo} [b] (F cm^{-3})[a]	$E_{d,vol}$ (mW cm^{-3})[a]	$E_{d,\ areal}$ (mW cm^{-2})[a]	$P_{d,vol}$ (mW cm^{-3})[a]	$P_{d,areal}$ (mW cm^{-2})
L1	14	2.15			—	
L2	1.8	0.28	8.0	5.0	2.0	0.16
L3	27	4.13	117	10	26	2.0

[a] V_{strip} = estimated single cell volume with reference to the strip between each couple of fingers infiltrated by the lignin: $V_{strip} = ø \times w \times l = 0.35$ cm × 10 μm × 200 nm); $V_{tot} = 90 \times V_{strip}$ estimated only for lignin displaying SC behavior. [b] Σ = lignin layer section crossed by the electric field lines: $\Sigma = ø \times l = 0.35 \times 200 \times 10^7$: value of the lignin layer section crossed by the electric field lines taken for the estimate of the areal parameters. $C_{vol} = C_p'$ (0.1 Hz)/V_{tot}; $C_{areal} = C_p'$ (0.1 Hz)/Σ; $E_{d,vol} = Q_{React}$ (0.1 Hz)/V_{tot}; $E_{d,areal} = Q_{React}$ (0.1 Hz)/Σ; $P_{d,vol} = P_{act}$ (0.1 Hz)/V_{tot} $P_{d,areal} = P_{act}$ (0.1 Hz)/Σ; ø: diameter of the IDE cell; w = finger gap; l = Ti/Au contact thickness; (see also the SI and the representative sketch in Fig. S8).

3 Conclusions

This study analyzed three different lignins (**L1**, **L2**, and **L3**) in response to an alternating electric field using Nyquist plots, broadband dielectric spectroscopy, and complex power representations. A correlation was found between the chemical, structural, and morphological properties and the electrical parameters such as AC conductivity, diffusivity, and mobility. Our analysis uses a consistent modeling framework for all lignins (shared BDS formalism and base EIS circuit), with a parsimony rule that adds a single LF diffusion/chemical term only when the data require it (*e.g.*, the Gerischer feature under bias in **L2**/**L3**). As a result, the comparison is done on model-robust metrics extrapolated directly from the data – the HF resistive intercept, the extent of capacitive dominance and its transition frequency, and BDS-derived mobility/diffusivity – rather than on fit-sensitive parameters. This makes the observed differences attributable to intrinsic material physics, not methodological choices. The results show that **L2** and **L3**, especially at 0.0 V DC, exhibit behavior similar to materials used in supercapacitors. **L1** shows a mixed behavior at both high and low frequencies, while **L2**, with its fibrous morphology, quickly transitions to an ideal capacitive state. **L3**, on the other hand, shows an intermediate behavior, similar to **L1** at high frequencies but dominated by capacitive effects at low frequencies. At 0.8 V, **L2** and **L3** show increased interaction with the external environment, supported by the presence of a Gerisher-type impedance, suggesting greater reactivity toward atmospheric gases. The reactivity of lignin appears to be linked to the OH content, particularly the aliphatic –OH groups. The BDS representations show how polymer structure influences reactivity and charge mobility, with **L3** exhibiting lower polymerization than **L1** and **L2**. AC conductivity varies based on morphology: **L1** exhibits delocalized ionic charge transport, while **L2** shows more localized transport. Impurities matter chiefly in high-ash lignins: **L2** (25.3%) exemplifies a regime where ashes promote mixed conduction and accelerate the capacitive-to-resistive transition, whereas in low-ash or ash-free materials ($\approx$0–3%) the dielectric and supercapacitive responses are dictated by hydroxyl/carboxyl chemistry and morphology. **L3** demonstrates a good balance of chemical and morphological properties, favoring strong ionic transport and capacitive performance. The comparative analysis presented herein on **L1**, **L2** and **L3** underscores that lignin performance is strongly influenced by its origin and extraction method. Commercial Kraft lignins provide industrially relevant benchmarks, while the organosolv **L3** offers higher purity and higher structural homogeneity. Selecting lignins with such contrasting structural and chemical characteristics enables evaluation across both abundant industrial feedstock and high-value reactive lignin, guiding the design of sustainable, next-generation electronic materials. The analysis of SC-related parameters in **L2** and **L3** together with the device configuration provided evidence that **L2** and **L3** exhibit complementary capacitive strengths and chemistry, aligning with benchmark capacitance values and high energy efficiency, offering a strong basis for future lignin-based microsupercapacitor development. The response similar to that of supercapacitors of **L2** and the chemically cleaner profile of **L3**, together with the higher estimated values of volumetric capacitance/energy/power, are directly reflected in two application paths: ready-to-use charge storage and purity-oriented dielectric-capacitive layers, respectively. The EIS fingerprints used here translate into practical acceptance criteria for large-scale coated devices. Therefore, our findings result into actionable quality assurance (QA) anchors, including incoming C_0 calibration and EIS-derived fingerprints used as pass/fail criteria within a defined operating window ($\pm$0.8 V). The established correlations between chemical composition and electrochemical performance enable the formulation of procurement specifications and batch ranking. Among the tested materials, organosolv lignin emerges as the most application-ready, while selected technical lignins also qualify, provided they meet defined thresholds for impurity levels and electrical performance.

Author contributions

M. A.: conceptualization, methodology, investigation, formal analysis, supervision, writing – original draft, writing – review & editing, funding acquisition. O. D.: investigation, formal analysis, supervision, writing – original draft, writing – review & editing. S. D. S.: investigation, data curation, writing – review & editing. R. D.: investigation, data curation, writing – review & editing. D. A.: investigation, data curation, writing – review & editing. P. F. A.: formal analysis, writing – review & editing, funding acquisition. N. M.: investigation, formal analysis, writing – review & editing. F. G.: investigation, formal analysis, writing – review & editing. S. R.: investigation, formal analysis, writing – review & editing, funding acquisition. A. O.: investigation, supervision, formal analysis, writing – original draft, writing – review & editing, funding acquisition. A. D. B.: supervision, formal analysis, writing – review & editing, funding acquisition.

Conflicts of interest

There are no conflicts to declare.

Data availability

The data supporting the findings of this study are available within the article and its supplementary information (SI) files. Supplementary information: detailed experimental procedures, characterization data (including elemental analysis, GPC, and ^{31}P-NMR spectroscopy), and electrical measurements (EIS, BDS, and Nyquist plots). Additional raw data and analysis files are available from the corresponding authors upon reasonable request. See DOI: **https://doi.org/10.1039/d5ta05024c**.

Acknowledgements

The authors are grateful to Prof. Anna Maria Raspolli Galletti and Prof. Franco Cotana for providing the steam exploded

cardoon. FE–SEM micrographs were acquired at the Center for Instrument Sharing of the University of Pisa (CISUP). A. D. B. and O. D. acknowledge the financial support from the University of Salerno, with grants ORSA223384 and ORSA235199. R. D. and A. O. acknowledge the University of Pisa for funding "BIHO 2022 – Bando Incentivi di Ateneo Horizon e Oltre" (Prot. n. 0048740/2022). S. R. acknowledges the funding from MCIN/AEI/10.13039/5011000 11033 and EU NextGeneration EU/PRTR (RYC2021-031964-I). S. R. and A. O. acknowledge the support from Consellería de Cultura, Educación, Formación Profesional y Universidades (Xunta de Galicia) (ED431F2023/03). M. A. and P. F. A. acknowledge the support from the Italian Ministry of University and Research (MUR) PONa3_00369 SISTEMA. P. F. A and D. A. acknowledge the support from Regione Puglia, Riparti – POC PUGLIA FESRT-FSE 2014/2020. D. A. thanks the Italian National Recovery and Resilience Plan (NRRP), funded by the European Union – NextGenerationEU (Mission 4, Component 2, Investment 3.1—Area ESFRI Energy—Call for tender No. 3264 of 28-12-2021 of Italian University and Research Ministry (MUR), Project IDIR0000007 'NEFERTARI'—MUR Concession Decree No. 243 del 04/08/2022, CUP B53C22003070006). Views and opinions expressed are however those of the author(s) only and do not necessarily reflect those of the European Union or the European Commission. Neither the European Union nor the European Commission can be held responsible for them. M. A. and P. F. A. also aknowledge the support from the Italian Minister of Economy and Finance (MEF) L. 234 del 30/12/2021 to CNR Project REACH-XY - Research actions for reducing the impact on agricultural and natural ecosystems of the harmful plantpathogen Xylella fastidiosa, CUP B93C22001920001.

References

1 Y. Park and J.-S. Lee, *ACS Appl. Mater. Interfaces*, 2017, **9**, 6207–6212.
2 V. K. Thakur, M. K. Thakur, P. Raghavan and M. R. Kessler, *ACS Sustainable Chem. Eng.*, 2014, **2**, 1072–1092.
3 T. Y. Nilsson, M. Wagner and O. Inganäs, *ChemSusChem*, 2015, **8**, 4081–4085.
4 C. Lai, Z. Zhou, L. Zhang, X. Wang, Q. Zhou, Y. Zhao, Y. Wang, X.-F. Wu, Z. Zhu and H. Fong, *J. Power Sources*, 2014, **247**, 134–141.
5 Y. She, X. Li, Y. Zheng, D. Chen, X. Rui, X. Lin and Y. Qin, *Energy Environ. Mater.*, 2024, **7**, e12538.
6 S. Kim, Y. K. Kim, H. Lee, S. B. Lee and H. S. Park, *ChemSusChem*, 2014, **7**, 1094–1101.
7 R. D'Orsi, C. V. Irimia, J. J. Lucejko, B. Kahraman, Y. Kanbur, C. Yumusak, M. Bednorz, F. Babudri, M. Irimia-Vladu and A. Operamolla, *Adv. Sustainable Syst.*, 2022, **6**, 2200285.
8 J. Zhu, C. Yan, X. Zhang, C. Yang, M. Jiang and X. Zhang, *Prog. Energy Combust. Sci.*, 2020, **76**, 100788.
9 W. E. Tenhaeff, O. Rios, K. More and M. A. McGuire, *Adv. Funct. Mater.*, 2014, **24**, 86–94.
10 W. Zhang, J. Yin, Z. Lin, H. Lin, H. Lu, Y. Wang and W. Huang, *Electrochim. Acta*, 2015, **176**, 1136–1142.
11 S. S. Khviyuzov and A. S. Volkov, *Polym. Adv. Technol.*, 2024, **35**, e6467.
12 S. Khviyuzov, K. Bogolitsyn, A. Volkov, G. Koposov and M. Gusakova, *Holzforschung*, 2020, **74**, 1113–1122.
13 S. De Stefano, O. Durante, R. D'Orsi, A. Operamolla, M. Ambrico, P. F. Ambrico, N. Martucciello, F. Giubileo and A. Di Bartolomeo, *J. Mater. Chem. C*, 2024, **12**, 13621–13631.
14 M. Khalid Rahmani, S. Ali Khan, M. Farooq Khan and M. Hee Kang, *J. Mater. Sci. Eng. B*, 2022, **282**, 115784.
15 R. D'Orsi, J. J. Lucejko, F. Babudri and A. Operamolla, *ACS Omega*, 2022, **7**, 25253–25264.
16 D. S. Bajwa, G. Pourhashem, A. H. Ullah and S. G. Bajwa, *Ind. Crops Prod.*, 2019, **139**, 111526.
17 S. Sethupathy, G. Murillo Morales, L. Gao, H. Wang, B. Yang, J. Jiang, J. Sun and D. Zhu, *Bioresour. Technol.*, 2022, **347**, 126696.
18 A. Sakakibara, *Wood Sci. Technol.*, 1980, **14**, 89–100.
19 H. Erdtman, *J. Polym. Sci., Part B*, 1972, **10**, 228–230.
20 C. J. Biermann, *Handbook of Pulping and Papermaking*, Elsevier, 1996.
21 S. Sharma, A. Sharma, S. I. Mulla, D. Pant, T. Sharma and A. Kumar, in *Lignin*, ed. S. Sharma and A. Kumar, Springer International Publishing, Cham, 2020, pp. 1–15.
22 D. Kai, M. J. Tan, P. L. Chee, Y. K. Chua, Y. L. Yap and X. J. Loh, *Green Chem.*, 2016, **18**, 1175–1200.
23 R. D'Orsi, N. Di Fidio, C. Antonetti, A. M. Raspolli Galletti and A. Operamolla, *ACS Sustainable Chem. Eng.*, 2023, **11**, 1875–1887.
24 B. R. Matos, R. Politano, J. F. Q. Rey, D. Hermida-Merino, U. Schade, L. Puskar and F. C. Fonseca, *Sci. Rep.*, 2018, **8**, 13441.
25 M. Ambrico, L. Guazzelli, A. Mezzetta, A. Cariola, L. Valgimigli, P. F. Ambrico and P. Manini, *J. Mol. Liq.*, 2024, **403**, 124892.
26 P. Frübing, F. Wang, T. F. Kühle and R. Gerhard, *Appl. Phys. A:Mater. Sci. Process.*, 2016, **122**, 1–10.
27 A. A. Khamzin, I. I. Popov and R. R. Nigmatullin, *Phys. Rev. E:Stat., Nonlinear, Soft Matter Phys.*, 2014, **89**, 032303.
28 J. E. B. Randles, *Discuss. Faraday Soc.*, 1947, **1**, 11.
29 K. A. Motovilov, V. Grinenko, M. Savinov, Z. V. Gagkaeva, L. S. Kadyrov, A. A. Pronin, Z. V. Bedran, E. S. Zhukova, A. B. Mostert and B. P. Gorshunov, *RSC Adv.*, 2019, **9**, 3857–3867.
30 R. D'Orsi, S. De Stefano, O. Durante, M. Ambrico, D. Aceto, F. Ambrico, N. Martucciello, F. Giubileo, S. Rivas, A. Amperomolla and A. D. B. Bartolomeo, *J. Phys. Mater.*, 2025, **8**, 045003.
31 *Impedance Spectroscopy: Theory, Experiment, and Applications*, ed. E. Barsoukov and J. R. Macdonald, Wiley, 1st edn, 2005.
32 A. L. Pomerantsev, *Progress in Chemometrics Research*, Nova Publishers, 2005.
33 B. Boukamp, *Solid State Ionics*, 2003, **157**, 29–33.
34 P. Johnson, *J. Chemom.*, 2005, **19**, 266–267.
35 P. L. Taberna, P. Simon and J. F. Fauvarque, *J. Electrochem. Soc.*, 2003, **150**, A292.
36 A. S. Bondarenko and G. A. Ragoisha, in *Progress in Chemometrics Research*, ed. , A. L. Pomerantsev, Nova Science Publishers, New York, 2005, pp. 89–102, the

program is available online at http://www.abc.chemistry.bsu.by/vi/analyser/.
37 P. Johnson, *J. Chemom.*, 2005, **19**, 266–267.
38 A. J. Bard and L. R. Faulkner, in *Electrochemical Methods: Fundamentals and Applications*, Wiley, New York Weinheim, 2nd edn., 2001.
39 A. S. Merenga, C. M. Papadakis, F. Kremer, J. Liu and A. F. Yee, *Colloid Polym. Sci.*, 2001, **279**, 1064–1072.
40 F. Fanari, C. Iacob, G. Carboni, F. Desogus, M. Grosso and M. Wilhelm, *LWT–Food Sci. Technol.*, 2022, **161**, 113345.
41 M. Nakanishi and A. P. Sokolov, *J. Non-Cryst. Solids*, 2015, **407**, 478–485.
42 B. Natesan, N. K. Karan and R. S. Katiyar, *Phys. Rev. E*, 2006, **74**, 042801.
43 M. Ambrico, A. B. Mostert, P. F. Ambrico, J. Phua, S. Mattiello and R. Gunnella, *J. Phys. D: Appl. Phys.*, 2024, **57**, 265303.
44 M. Wübbenhorst and J. Van Turnhout, *J. Non-Cryst. Solids*, 2002, **305**, 40–49.
45 B. R. Matos, R. Politano, J. F. Q. Rey, D. Hermida-Merino, U. Schade, L. Puskar and F. C. Fonseca, *Sci. Rep.*, 2018, **8**, 13441.
46 E. M. Trukhan, *Soviet Phys. Solid State*, 1963, **4**(12), 2560–2570.
47 J. Yuval and S. A. Safran, *Phys. Rev. E:Stat., Nonlinear, Soft Matter Phys.*, 2013, **87**, 042703.
48 A. K. Jonscher, *Nature*, 1977, **267**, 673–679.
49 T. S. Sørensen and V. Compañ, *J. Chem. Soc., Faraday Trans.*, 1995, **91**, 4235–4250.
50 K. Funke, *Prog. Solid State Chem.*, 1993, **22**, 111–195.
51 A. K. Jonscher, *J. Phys. D: Appl. Phys.*, 1999, **32**, R57–R70.
52 A. Lisý, A. Ház, R. Nadányi, M. Jablonský and I. Šurina, *Energies*, 2022, **15**, 6213.
53 F. W. Zerban and L. Sattler, *Ind. Eng. Chem., Anal. Ed.*, 1931, **3**, 41–43.
54 M. J. Kim, M. Kim, W. B. Sohn, J. Kang, W. Kim and J. G. Kang, *Adv. Energy Mater.*, 2024, **14**, 2402322.